Journal of Alloys and Compounds 519 (2012) 112–122

Contents lists available at SciVerse ScienceDirect

Journal of Alloys and Compounds

journal homepage: www.elsevier.com/locate/jallcom

Microstructural, magnetic and optical characterizations of nanocrystalline $Zn_{1-x}Mn_xO$ dilute magnetic semiconductors synthesized by mechanical alloying

S. Sain [a], J. Bhattacharjee [a,1], M. Mukherjee [b], D. Das [c], S.K. Pradhan [a,*]

[a] Department of Physics, The University of Burdwan, Golapbag, Burdwan-713104, West Bengal, India
[b] Surface Physics Division, Saha Institute of Nuclear Physics, Bidhannagar, Kolkata-700064, India
[c] UGC-DAE Consortium for Scientific Research, Kolkata-700098, India

ARTICLE INFO

Article history:
Received 11 November 2011
Received in revised form
22 December 2011
Accepted 23 December 2011
Available online 31 December 2011

Keywords:
Nanostructured materials
Microstructure
X-ray diffraction
TEM
Magnetic measurements

ABSTRACT

Nanocrystalline Mn doped $Zn_{1-x}Mn_xO$ ($x = 0.02, 0.05, 0.07, 0.10$) dilute magnetic semiconductors (DMSs) have been synthesized by mechanical alloying the stoichiometric mixtures of ZnO and MnO powders for different durations in a high energy planetary ball mill at room temperature under air medium. In the course of milling, the peak broadening of ZnO reflections increases continuously and MnO reflections disappear completely after 2 h of milling. Microstructure characterization of ball milled samples employing the Rietveld structure refinement using X-ray diffraction data reveals that the Zn^{2+} ions are replaced by Mn^{2+} ions and lattice parameters of ZnO matrix increase slowly due to this substitution. Particle size of these DMS decreases continuously with increasing Mn concentrations. XPS measurement indicates that the doped Mn ions possess both Mn^{2+} and Mn^{4+} valance states. Magnetic characterization of DMS samples shows room temperature ferromagnetism (RTF), which confirms the inclusion of Mn^{2+} in ZnO lattice and the RTF can be explained in the light of RKKY exchange interaction. Optical characterization of these DMS by UV–vis spectroscopy clearly reveals a red-shift and consequently the optical band-gap decreases with increasing Mn concentrations.

1. Introduction

The dilute magnetic semiconductors (DMS) offer the advantages of semiconductors combined with properties of magnetic materials. The ZnO based DMS systems have some unique characteristics like large band gap (~3.37 eV), large exciton binding energy at room temperature (~60 meV), high optical gain (300 cm^{-1}), very short luminescence life time [1] which are required for various optoelectronic [2] and magneto-optical [3] devices.

The manufacturability of these materials depends on thermal equilibrium solubility of the dopant in the base material. The II–VI, III–V group elements are the most studied materials. Enormous application of spintronic devices such as spin-valve transistor, spin-light emitting diodes, non-volatile memory, optical isolator and ultra fast optical switches inspired widespread research work to synthesize the DMS with II–VI and III–V semiconductors [1–16]. Among these materials, Mn doped II–VI and III–V semiconductors have been well studied, particularly the Mn doped GaAs [4,5]. However, the Curie temperatures (T_C) of these materials have been limited to 140 K which is very low for practical device applications [17]. The maximum ferromagnetic Curie temperature (T_C) reported for this system is ~172 K which is much lower than room temperature [18]. Dietl et al. [19] predicted that magnetically doped wide band-gap p-type semiconductors particularly ZnO and GaN can achieve Curie temperature well above the room temperature. This fact has motivated researchers to study the properties of transitional metal doped semiconductors. Milivojević et al. [13] prepared ferromagnetic polycrystalline $Zn_{1-x}Mn_xO$ samples at room temperature by solid state sintering route. Jayakumar et al. [7] reported the room temperature ferromagnetism in polycrystalline Mn doped ZnO synthesized by low temperature solid state reaction of MnO_2 and ZnO. But in none of the previous cases, MnO has been considered as the dopant to ZnO, though it would be a better way of substitution of Zn^{2+} by Mn^{2+} as both of the ions have same valence state and also very close ionic radii.

In the present work, Mn-doped ZnO nanocrystalline DMS powders have been synthesized for the first time by mechanical alloying the ZnO and MnO powders within 2 h of milling duration and sincere efforts have been made for microstructure characterization, magnetic and optical property measurements using X-ray powder diffraction (XRD), high resolution transmission electron microscope (HRTEM), X-ray photoluminescence spectroscopy (XPS), superconducting quantum interface device (SQUID) and UV–vis spectrometer. Structural and microstructure characterizations are made by analyzing the XRD data employing the Rietveld method

* Corresponding author. Tel.: +91 342 2657800; fax: +913422530452.
E-mail address: skp_bu@yahoo.com (S.K. Pradhan).
[1] Dept. of Physics, Tripura Universiy, Tripura-799 022, India.

0925-8388/$ – see front matter © 2012 Elsevier B.V. All rights reserved.
doi:10.1016/j.jallcom.2011.12.132

of structure and microstructure refinement and HRTEM. The room temperature ferromagnetic behavior of these prepared samples is revealed from M-H loop traced by SQUID and the optical band gap is measured from the UV–vis absorption spectra. The objectives of the present work are to (i) prepare Mn-doped ZnO using MnO as dopant, (ii) find an easiest and quickest way for nanocrystalline ZnO DMS preparation, (iii) characterize these DMS by several methods to ascertain room temperature ferromagnetism in Mn-doped ZnO, and (iv) determine the variation of band gap with the variation of doping concentration.

2. Experimental

The nanocrystalline $Zn_{1-x}Mn_xO$ (x = 0.02, 0.05, 0.07, 0.10) samples were synthesized by mechanical alloying (MA) the metal oxide precursors. Initially, the stoichiometric mixtures of pure ZnO (E. Merck; purity 99%) and MnO (Alpha Aser; purity 99.5%) powders were mixed in different molar ratios in an agate mortar for 30 min. Then milling of powder mixture was performed in a high-energy planetary ball mill (Model-P5, M/s FRITSCH, GmbH, Germany) in air medium at room temperature in a chrome steel vial of 80 ml volume filled with chrome steel balls of 10 mm diameter. Different Mn doped $Zn_{1-x}Mn_xO$ DMS samples were prepared by ball milling the powder mixtures for 0.5, 1 and 2 h durations.

Structure and microstructure of these samples were primarily characterized by X-ray diffraction (XRD) using Ni-filtered CuK_α radiation from an X-ray powder diffractometer (Panalytical; Model PW1830) operated at 40 kV and 20 mA. For detailed X-ray line profile analysis employing the Rietveld's method of structure and microstructure refinement, step-scan data (of step size 0.02° 2θ and counting time 30 s) of unmilled and all ball milled samples were recorded for the entire angular range 20°-80° 2θ. Microstructure of 2 h ball milled sample was also characterized by HRTEM (JEOL JEM 2010) equipped with GATAN CCD camera operated at 200 kV to verify the results obtained from X-ray analysis. A pinch of sample was dispersed in ethanol, sonicated for a long time and subsequently, a drop of it was put on a carbon coated copper grid for TEM study.

In order to analyze the chemical states of the constituent elements, XPS measurements were performed with an emphasis on the peaks associated with Zn 2p and Mn 2p. XPS core-level spectra were recorded with an Omicron Multiprobe (Omicron NanoTechnology GmbH., UK) spectrometer fitted with an EA125 hemispherical analyzer. A monochromatic Al K_α X-ray source operated at 150 W was used for the experiments. The analyzer-pass energy was kept fixed at 40 eV for all the scans. As the samples are insulating in nature, a low energy electron gun (SL1000, Omicron) with a large spot size was used to neutralize the samples. The potential of the electron gun was kept fixed at −3 eV for all the samples with respect to the ground. The binding energies of the peaks were corrected by shifting the peak positions by an equal amount that was required to shift the main peak of the corresponding C1s spectrum to 285.0 eV.

The variation of band gap with concentration of doping material was investigated by UV–vis absorption spectroscopy using a Shimadzu UV–vis spectrometer (Shimadzu UV–vis 1800) in the wavelength range (200–800) nm at room temperature.

The magnetic properties of the milled samples were measured by a SQUID magnetometer (MPMS XL 7, fitted with an evercool dewar, supplied by Quantum Design, USA). In order to observe the variation of the hysteresis loop and the magnetic ordering between the as prepared (2 h ball milled) sample and its annealed counterpart, DC magnetization loop of annealed (at 773 K for 3 h) powder is also recorded at room temperature.

3. Method of analysis

In the present study, we have adopted the Rietveld's powder structure refinement method [20–30] for X-ray powder diffraction data analysis to obtain the structural parameters, such as atomic coordinates, occupancies, lattice parameters, thermal parameters, etc. and microstructure parameters such as particle size and r.m.s. lattice strain of Mn doped ZnO DMS samples. The Rietveld's software MAUD 2.26 [24] is specially designed to refine simultaneously both the structural and microstructure parameters through Marquardt least-squares method. The peak shape is assumed to be a pseudo-Voigt function with asymmetry because it takes individual care for both the particle size and strain broadening of the experimental profiles. The background of each pattern is fitted by a polynomial of degree four. The theoretical X-ray powder diffraction pattern is simulated containing ZnO and MnO phases in a single pattern as the patterns are composed of reflections from these phases.

Initially, positions of all peaks are corrected by successive refinements of zero-shift error. Considering the integrated intensity of the peaks as a function of structural and microstructural parameters, the Marquardt least-squares procedure is adopted for minimizing the difference between the observed and simulated powder diffraction patterns and the minimization is monitored using the reliability index parameter, R_{wp} (weighted residual error) and R_{exp} (expected error) defined, respectively, as

$$R_{wp} = \left[\frac{\sum_i w_i(I_0 - I_c)^2}{\sum_i w_i(I_0)^2}\right]^{1/2}$$

$$R_{exp} = \left[\frac{N - P}{\sum_i w_i(I_0)^2}\right]^{1/2}$$

where I_0 and I_c are the experimental and calculated intensities, $w_i(=1/I_0)$ and N are the weight and number of experimental observations, and P is the number of fitting parameters. This leads to the value of goodness of fit (GoF): [20–25]

$$GoF = \frac{R_{wp}}{R_{exp}}$$

The peak broadening, peak asymmetry and peak shift of the experimental profiles are fitted by refining the particle size, lattice strain and lattice parameter values (including zero-shift error). Refinements of all parameters are continued until convergence is reached with the value of the quality factor, GoF very close to 1 (varies between 1.1 and 1.3), which confirms the goodness of refinement. Microstructure parameters such as particle size, lattice strain values of ball-milled samples are obtained from this analysis along with all structural parameters. It may be noted that the Cagliotti parameters U, V, and W [23] instrumental asymmetry and Gaussianity parameters [24] are obtained for the instrumental setup using a specially prepared Si standard and kept fixed during refinements.

4. Results and discussion

4.1. Nanostructure characterization by XRD and HRTEM

X-ray powder diffraction patterns of unmilled and all ball-milled $Zn_{1-x}Mn_xO$ samples with x = 0.02, 0.05, 0.07 and 0.10 milled for different durations look quite similar and the end compositions are shown in Fig. 1(a) and (b). In these figures, all unmilled (0 h) mixtures are composed of ZnO and MnO reflections only. All reflections are well resolved and at higher scattering angle split clearly into $CuK_{\alpha 1-\alpha 2}$ doublets. It indicates that particle sizes of both starting ingredients are quite large and they are almost free from lattice strain.

In the course of milling time up to 1 h, peak broadening of all reflections increases continuously, or else, there is no significant change noticed in the XRD patterns of ball-milled samples. Just after another 1 h of milling, MnO reflections disappear completely in the XRD patterns of all compositions. As there is no change in ZnO reflections except peak broadening, it indicates that the Mn^{2+} ions in all proportions are incorporated easily into the ZnO lattice. It further suggests that the solubility limit of MnO in ZnO is more than 10 mol.%. The newly formed phase can be treated as the (Zn,Mn)O solid solution. In most of the earlier cases, MnO_2 was used as dopant and Zn^{2+} ions (r = 0.75 Å) in tetrahedral coordination were replaced by Mn^{2+} (r = 0.85 Å) ions. In some cases, room temperature ferromagnetic behavior in Mn-doped ZnO was assigned due to the ferromagnetic cluster. However, in the present study, we did not notice the presence of any new phase or cluster in any of the compositions milled up to 2 h of milling. It confirms that the ZnO is a

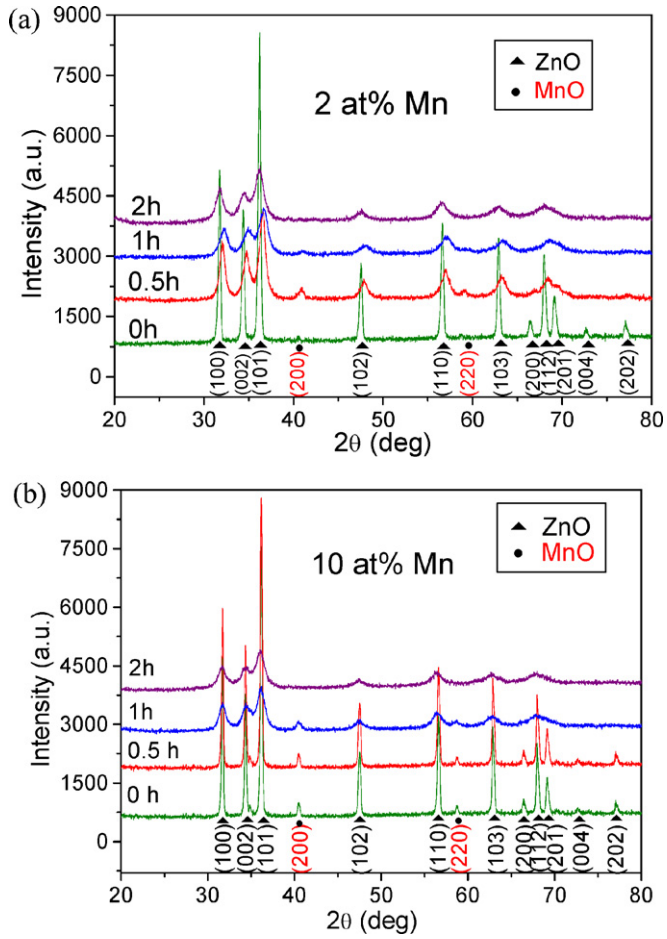

Fig. 1. XRD patterns of ZnO and MnO mixtures milled for different durations (a) $Zn_{0.98}Mn_{0.02}O$ and (b) $Zn_{0.90}Mn_{0.10}O$.

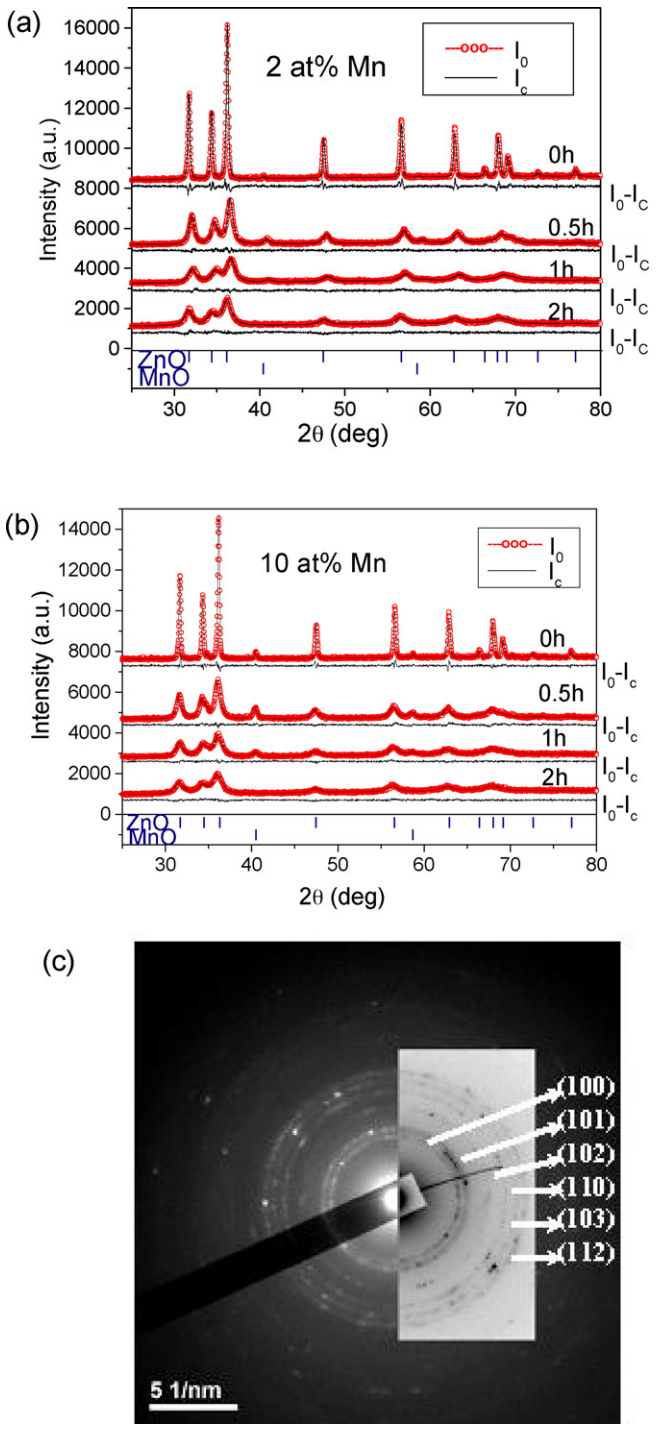

Fig. 2. Typical Rietveld analysis output of the XRD patterns of ZnO and MnO mixtures milled for different durations (a) $Zn_{0.98}Mn_{0.02}O$ and (b) $Zn_{0.90}Mn_{0.10}O$. Experimental (I_O) data are shown as (o), simulated patterns (I_C) are shown by solid lines, (I_O–I_C) represents the corresponding difference for each of the pattern, (c) indexed selected area electron diffraction (SAED) pattern of 2 h ball milled $Zn_{0.90}Mn_{0.10}O$ nano-particles.

stable phase material and its structure remains invariant up to 2 h of milling.

It is well known that properties of any crystalline material change with changing its microstructure. If it is possible to evaluate the microstructure parameters related to lattice imperfections by any means, then by controlling the microstructure parameters, a control over properties can be achieved and a 'tailor-made' material with desirable properties may be prepared. To evaluate the microstructure of the ball milled samples in terms of different lattice imperfections like, change in lattice parameter, particle size and lattice strain, the Rietveld method of structure refinement has been adopted in the present case, as this is one of the best methods for microstructure characterization of samples having significant number of overlapping reflections. This method is also able to estimate quantitatively the relative phase abundances in a multiphase material. In the present study, the simulated XRD patterns for the Rietveld analysis are generated with the following phases: ZnO (ICSD – 65121, Sp. Gr. $P6_3mc$, hexagonal, $a = 3.25682$ Å; $c = 5.21251$ Å), and MnO (ICSD – 643195, Sp. Gr. $Fm\bar{3}m$, cubic, $a = 4.4440$ Å) phases.

Experimental XRD patterns of unmilled and all ball-milled samples of all compositions are fitted very well by refining the structural and microstructure parameters of respective simulated patterns and the fitted XRD patterns of end compositions are shown in Fig. 2(a) and (b). XRD patterns of 2 h milled samples of all compositions are fitted very well with (Zn,Mn)O solid solution consideration where Zn^{2+} ions are replaced by subsequent amount of Mn^{2+} ions. The 'goodness of fittings' (GoFs) in all cases lie in between 1.1 and 1.3 which signify that the fitting qualities are good enough for all experimental patterns. The residual of fittings (I_O–I_C) between observed (I_O) and calculated (I_C) intensities of each fitting is plotted under respective XRD patterns. Peak positions of all reflections of these two phases are marked (|) and shown at the bottom of the plot. It is clearly evident from the plot that the (Zn,Mn)O solid solution is formed within 2 h of milling without any contamination from neither of precursor

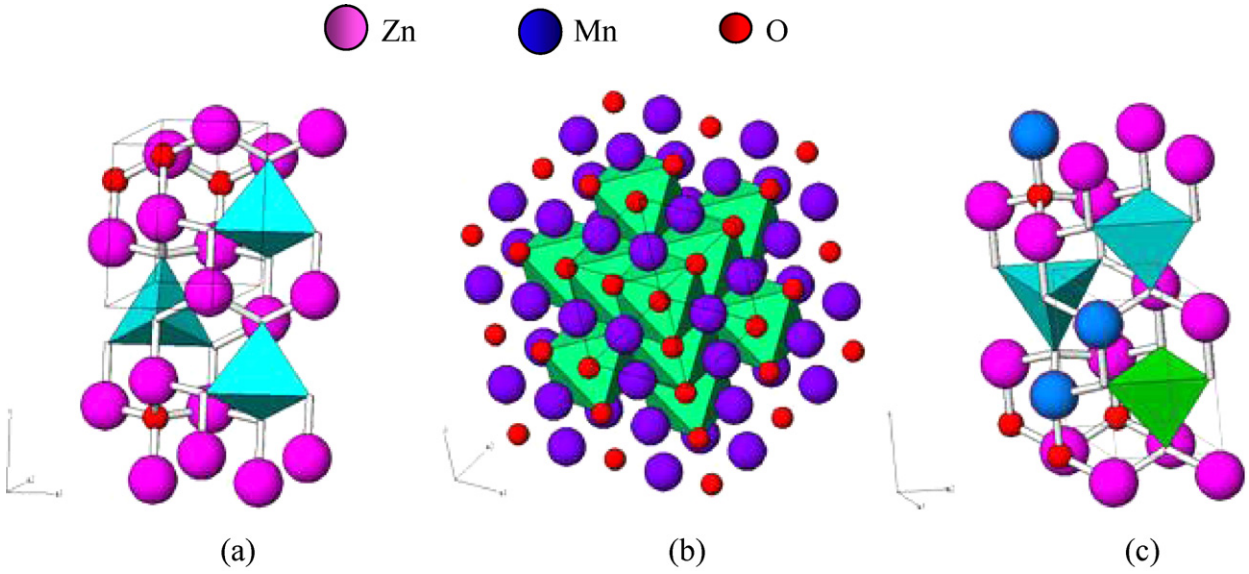

Fig. 3. Structures of (a) ZnO (wurzite), (b) MnO (cubic) and (c) ZnO:Mn (wurzite), respectively.

powders nor from the milling media. But, a careful observation of isolated (1 0 2) reflections at ~47.7° 2θ in all compositions indicates that the peak-broadening increases continuously with increasing Mn-concentration. It signifies that lattice imperfections in ZnO matrix increases with increasing atomic size mismatch between Zn^{2+} (r = 0.75 Å) and Mn^{2+} (r = 0.85 Å) ions and manifested in substitutional solid solution. The observation of X-ray data analysis agrees well with HRTEM image where the presence of ZnO phase is shown clearly in $Zn_{0.9}Mn_{0.1}O$ sample after 2 h of milling by indexing selected area electron diffraction (SAED) pattern (Fig. 2(c)). We did not notice the presence of any Mn-oxide phase (MnO, MnO_2, Mn_2O_3 Mn_3O_4 or $ZnMn_2O_4$ phase) within this duration of milling which had been noticed by Karamat et al. [31] and other researchers [32–34].

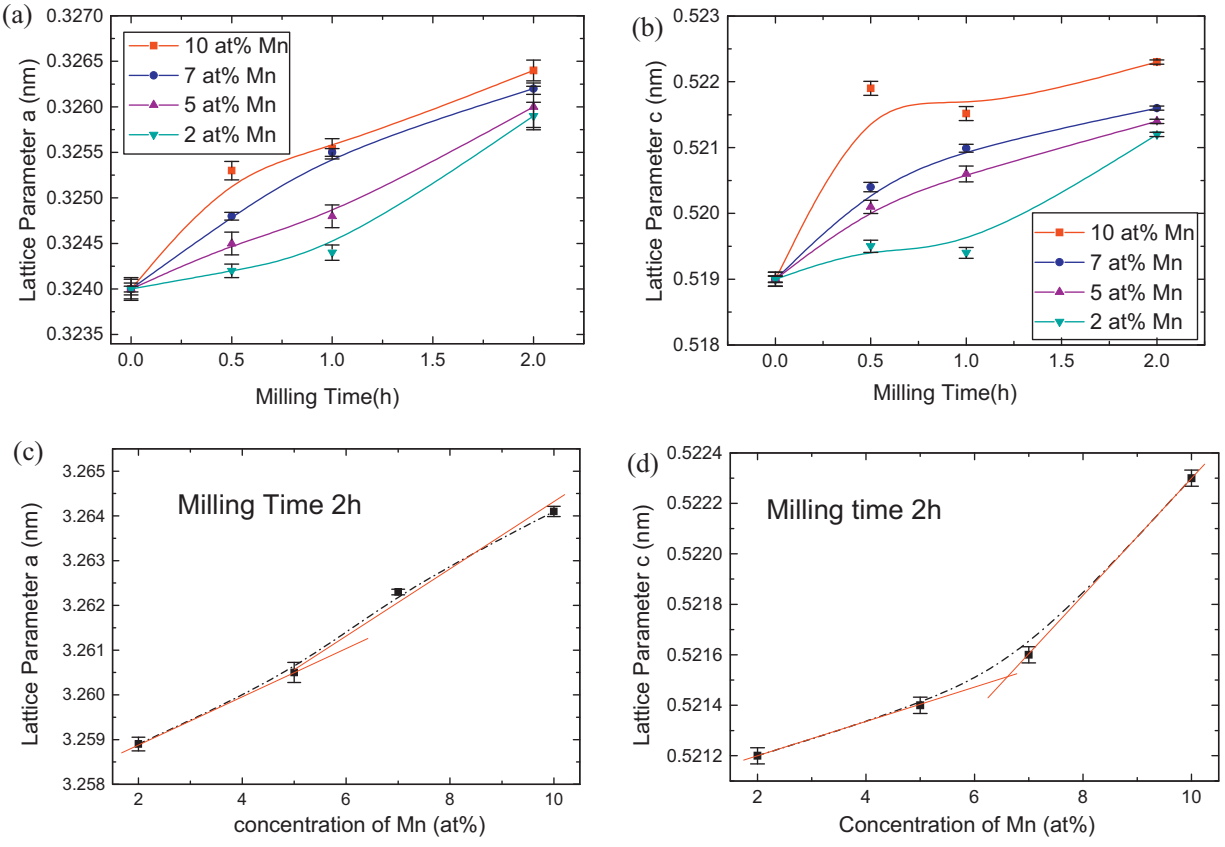

Fig. 4. Lattice parameter variations of ZnO and MnO mixtures milled for different durations (a) variation of '*a*' with increasing milling time for different compositions, (b) variation of '*c*' with increasing milling time for different composition, (c) increment of '*a*' with increasing Mn concentration, and (d) increment of '*c*' with increasing Mn concentrations.

Fig. 3 shows the crystal structures of ZnO (ICSD – 65121), MnO (ICSD – 643195) and ZnO:Mn lattices, respectively. The primitive unit cell and orientation of the crystallographic axes for each of the structure have been shown in the figures. Periodic arrangement of Zn (magenta) and Mn (blue) tetrahedrons in respective figures indicates these lattices are undistorted. The structure of ZnO:Mn is the same as that of pure ZnO except some Zn atoms (fractional coordinates 1/3, 2/3, 0) have been replaced by Mn atoms and a (Zn,Mn)O substitutional solid solution is formed due to Mn doping. As the ionic radii of Mn^{2+} and Zn^{2+} are close, tetrahedrons remain undistorted due to this substitution reaction.

Variations of lattice parameters '*a*' and '*c*' of ZnO phase with increasing milling time in all compositions are shown in Fig. 4(a) and (b), respectively. Both the parameters increase in general, non-linearly with increasing milling time which indicates the gradual diffusion of Mn^{2+} into ZnO lattice. These lattice parameters are also increasing continuously (Fig. 4(c) and (d)) with increasing Mn concentrations, signify the constant substitution of Zn^{2+} ions by the bigger Mn^{2+} ions during solid solution formation following the Vegards's law for substitutional alloys. Several authors [35–37] reported the variation of ZnO lattice parameters with increasing Mn concentrations in Mn-doped ZnO DMS. However, the gradual changes in lattice parameters on the way to complete formation of (Zn,Mn)O DMS in the course of milling are revealed for the first time by the Rietveld analysis of XRD data of all ball-milled samples. It may also be noted that both the lattice parameters increase in two steps and increment of '*c*' is higher than '*a*' at higher Mn concentrations. It indicates that Mn^{2+} ions could perfectly substitute smaller Zn^{2+} ions preferably on *c*-axis.

The relative phase abundance of (Zn,Mn)O phase in unmilled and ball-milled samples are obtained from the Rietveld analysis of XRD data of respective samples and shown in Fig. 5(a). It may be noted that initially the phase content of ZnO phase decreases in all compositions within 30 min of milling and then increases slowly to complete the solid-solution formation process. This decrease indicates the increase of MnO phase content which may be attributed to diffusion of ZnO phase into MnO lattice and a MnO-based solid solution is formed at the early stage of milling. Diffusion of ZnO phase into MnO lattice is very much evident from Fig. 5(b). Critical analysis of the XRD pattern of unmilled mixture of ZnO and 5 mol.% MnO powders reveals the ratio of the intensities (peak heights) of (1 0 2) of ZnO and (2 0 0) of MnO phases as ~5.4507 and that for 30 min milled sample is found to be ~0.9846. This decrease in intensity ratio of these two phases confirms the inclusion of ZnO phase into the MnO lattice at the initial stage of milling. Similarly, in case of unmilled mixture of ZnO and 7 mol.% MnO powders, these intensity ratios are 4.5685 and 0.9243 respectively. In the course of milling, finally the ZnO-based solid solution is formed.

The Rietveld analysis reveals that particles are isotropic in nature and in the course of milling, particle sizes of (Zn,Mn)O in all compositions reduce very rapidly and their variations with increasing milled time are shown in Fig. 6(a). It may be noted that the particle sizes in all compositions reduce to ~6.5 nm after 2 h of milling. However, a careful observation (as shown in the inset of Fig. 6(a)) clearly reveals the rate of decrease in particle sizes with Mn concentrations. At the final stage, i.e. after 2 h of milling, particle size of 2 at.% Mn doped ZnO composition particle size rapidly reduces to ~7.2 nm but in case of 10 at.% Mn doped ZnO composition particle size rapidly reduces to ~6.4 nm. It indicates that increase in Mn concentrations results in particle size reduction in presence of lattice imperfections originated from the atomic size mismatch between Zn^{2+} and $Mn2^{+}$ ions. The average particle size obtained from HRTEM analysis of $Zn_{0.9}Mn_{0.1}O$ composition milled for 2 h is ~7 nm. The average size of spherical particles (marked with white circles) in 2 h milled sample is estimated from the TEM images (Fig. 6(b) and (c)) and the size of these particles vary

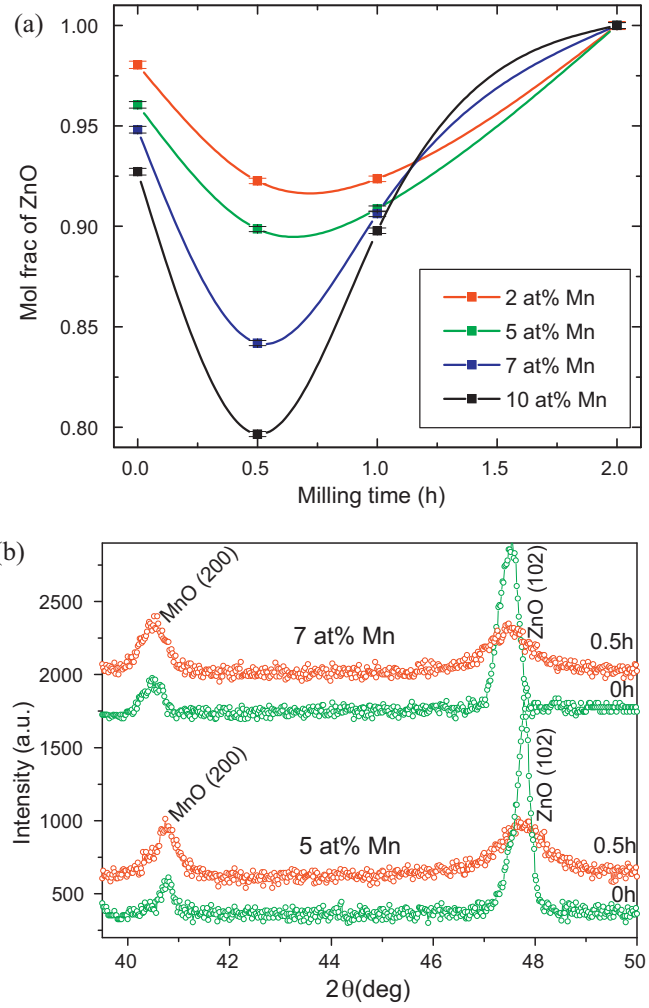

Fig. 5. (a) Variations of mole fractions of ZnO in ZnO and MnO mixtures ($x = 0.02$, 0.05, 0.07, 0.10) milled for different durations, (b) comparisons of peak intensities of ZnO and MnO phases between 0 h and 0.5 h milled samples for $x = 0.05$ and 0.07.

between ~6.0 and 7.5 nm. However, most of the particles are spherical in shape and their average size is ~7 nm. The distribution of particle size is represented in a histogram (Fig. 6(d)) where it can be seen that particles are almost mono-dispersed with average size lying between 6.5 and 7.0 nm, which is very close to that obtained from X-ray analysis. A very close look at the bright field HRTEM images in Fig. 7(a)–(d) reveals the particle size of 2 h milled powders. Fig. 7(a) shows few particles in the 10 at.% Mn doped ZnO sample. The interplanar spacing of these particles (Fig. 7(b)) is ~2.49 Å which confirms the presence of (1 0 1) plane of $Zn_{0.9}Mn_{0.1}O$ phase. Size of this particle is ~5.8 nm. In Fig. 7(c) bright field HRTEM image reveals clearly an individual spherical particle with clear lattice fringes, and it is identified as the (1 0 1) plane of $Zn_{0.9}Mn_{0.1}O$ phase. Fig. 7(d) shows another particle in magnified form with particle size is ~7 nm and the interplanar distance ~2.6 Å confirms the presence of (0 0 2) plane of $Zn_{0.9}Mn_{0.1}O$ phase. Lattice fringes as shown in Fig. 8(a) and (b), taken from another area reveal the presence of (0 0 2), (1 1 0) and (1 0 1) atomic planes of $Zn_{0.9}Mn_{0.1}O$ phase. Absence of any atomic plane of dopant MnO confirms the complete inclusion of Mn^{2+} in Zn^{2+} lattice sites. As the atomic planes are perfectly parallel, therefore, the occurrence of stacking faults in these nano particles may be ruled out.

The r.m.s. lattice strain generated in the (Zn,Mn)O matrix during the milling has been obtained from the Rietveld analysis and shown in Fig. 9. It is evident from the variation that the lattice strain in all

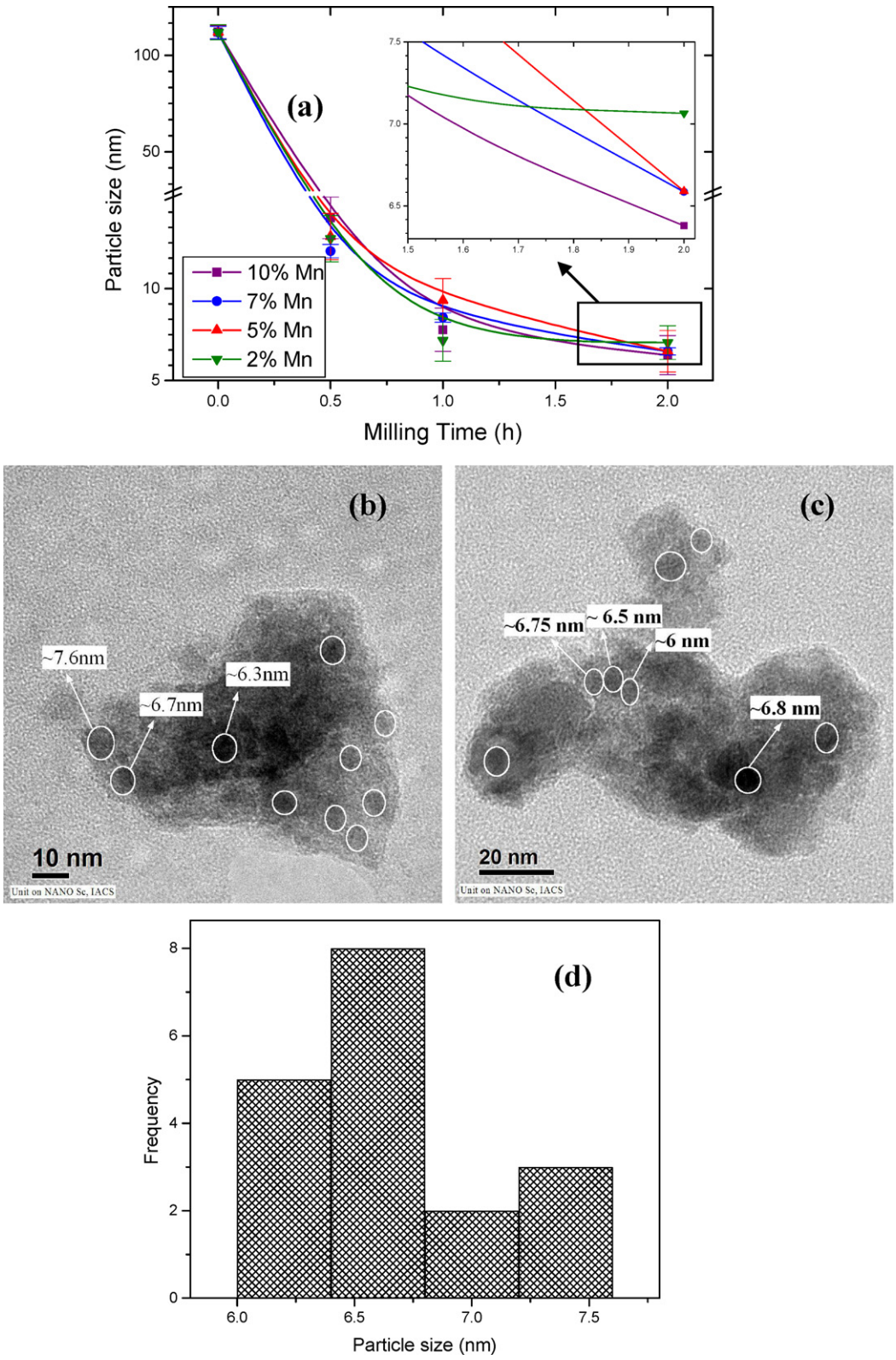

Fig. 6. (a) Variation of particle sizes of ZnO in ZnO and MnO mixtures with increasing milling time with varying Mn concentrations, (b) and (c) spherical particles in the TEM images of 2 h milled nanocrystalline $Zn_{0.90}Mn_{0.10}O$ powders are shown with white circles, and (d) particle size distribution of 2 h milled $Zn_{0.90}Mn_{0.10}O$ powders represented by histogram.

compositions increases continuously with increasing milling time. This increasing nature of strain signifies that in the course of milling, more and more Zn^{2+} ions are substituted by larger Mn^{2+} ions (Fig. 9 inset).

The distributions of particle sizes with increasing milling time for all compositions are obtained from the Rietveld analysis. Nature of the distribution in all compositions is similar and one of them is shown in Fig. 10(a). It is evident from the variations that

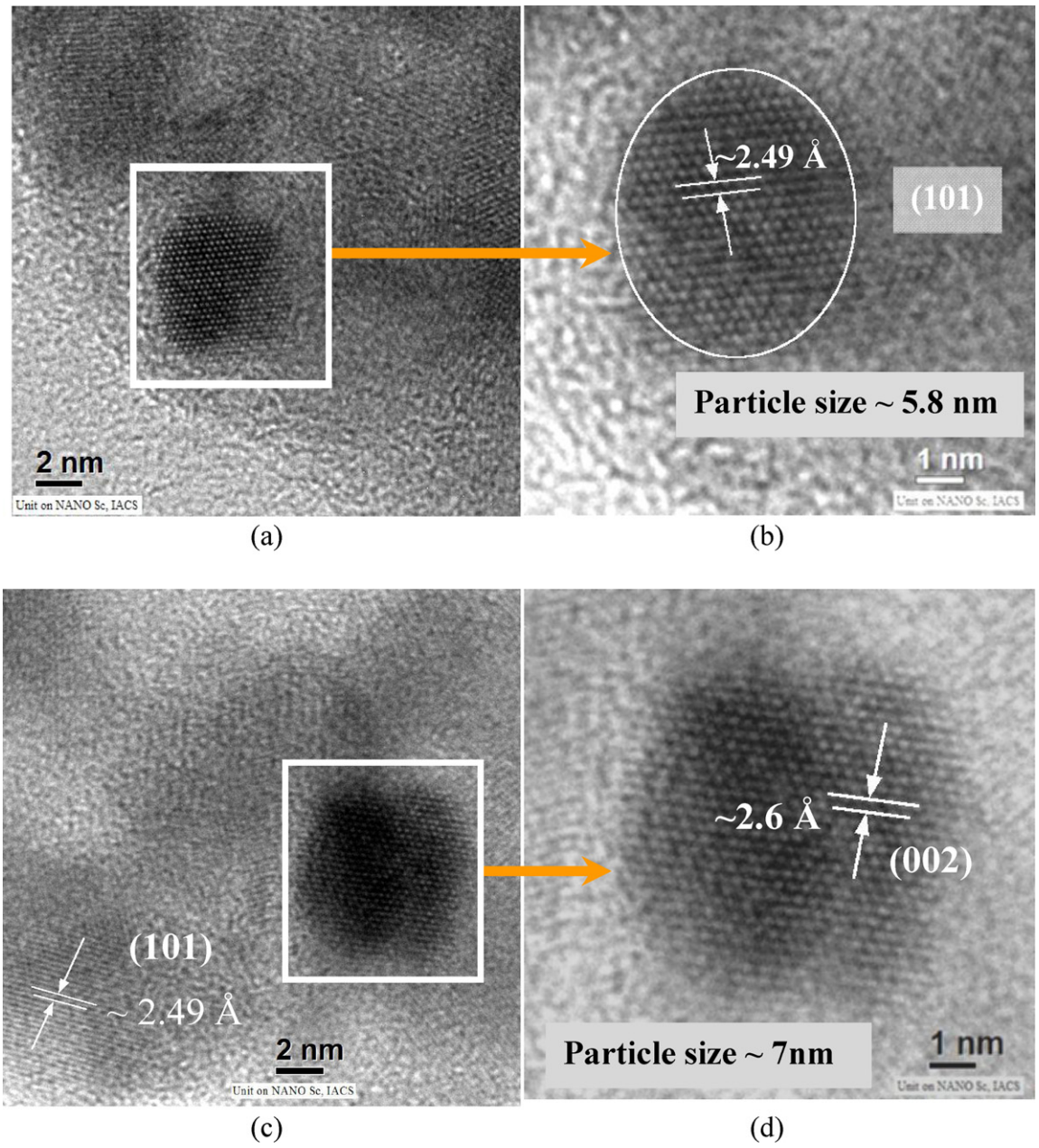

Fig. 7. (a) and (c) HRTEM images of $Zn_{0.9}Mn_{0.10}O$ nano particles. Fig. 7 (b) and (d) shows distinct particles of $Zn_{0.90}Mn_{0.10}O$ phase with some of measured interplanar distances.

particle size distribution reduces continuously and after 2 h of milling almost monodispersed particles are obtained, which is also evident from HRTEM images (Fig. 6(b) and (c)). The distributions of lattice strains of all of compositions have also been obtained from the Rietveld analysis. However, the nature of distributions is similar for all the compositions. Nature of variation of one such composition ($Zn_{0.95}Mn_{0.05}O$) is shown in Fig. 10(b). As the particle size reduces with milling time, the concentration of lattice strain increases, which signifies that smaller particles contain more strain.

4.2. XPS measurements

Fig. 11 represents the typical Zn 2p and Mn 2p XPS spectra of the 10 at.% Mn-doped ZnO nano powders. Fig. 11(a) shows the Zn $2p_{3/2}$ XPS spectra of the sample. Although the data appear to be a single peak but it is observed that two peaks are required to fit the data in a better manner. The peak at 1021.8 eV of ~70% intensity matches very well with the binding energies of ZnO and the another close to 1022.7 eV may be due to the presence of 30% ZnO in a different environment of $Zn(OH)_2$ which may have formed as thin film on the sample surface due to water adsorption. The presence of $Zn(OH)_2$ in Mn-doped ZnO samples has been reported earlier [38]. It may be noted that the presence of $Zn(OH)_2$ is not noticed in the XRD patterns due to its insignificant contribution or in its presence in amorphous state in the form of thin film. The incorporation of Mn into the ZnO lattice can be clearly demonstrated by the core level spectra of Mn $2p_{3/2}$ (Fig. 11(b)). Here again, the data appear to consist of a single peak but the proper fitting is obtained after considering two Gaussian–Lorentzian sum functions. Positions of these peaks appear at 641.1 eV and 642.7 eV and they are assigned to Mn^{2+} and Mn^{4+}, respectively. A quantitative analysis reveals the relative percentage of Mn^{2+} and Mn^{4+} to be ~20% and ~80%, respectively. These results indicate that the doped Mn ions possess two different valance states, Mn^{2+} and Mn^{4+}, respectively and the presence of Mn^{2+} ions results in observed room temperature

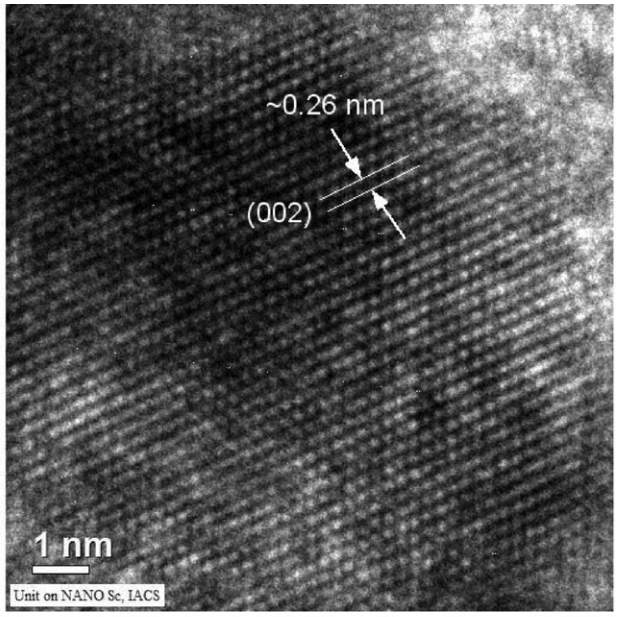

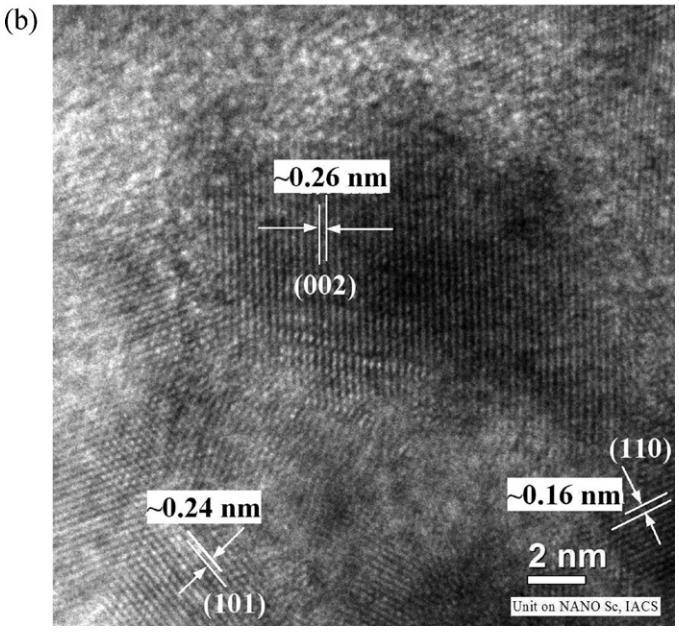

Fig. 8. (a) and (b) HRTEM images of 2 h milled $Zn_{0.9}Mn_{0.1}O$ sample confirming the presence of (0 0 2), (1 0 1) and (1 1 0) lattice planes of $Zn_{0.90}Mn_{0.10}O$ phase.

ferromagnetism in these samples which is already established by several research groups [6,39].

4.3. Magnetic characterization

The DC magnetization loops of ball milled (room temperature) and annealed (at 773 K for 3 h) $Zn_{0.98}Mn_{0.02}O$ powders are represented in Fig. 12. It can be seen that both the samples show 'S' shaped loops indicating their ferromagnetic nature. Both samples show (inset) clear hysteresis loops with coercive field $H_c \sim 75$ Oe and remanence M_r of 2.2×10^{-4} emu for room temperature sample and $\sim 1.7 \times 10^{-4}$ emu for the annealed sample. DC magnetization loops of these samples indicate that practically there is no signature of magnetic saturation even at higher magnetic fields. It appears that there are some paramagnetic and superparamagnetic components along with the definite ferromagnetic ordering which gives monotonically increasing magnetization with increase of magnetic

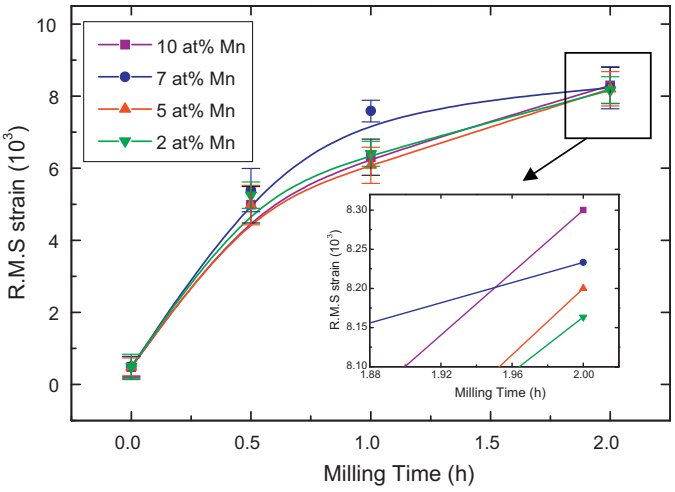

Fig. 9. Variation of lattice strain of ZnO with increasing milling time with varying Mn concentrations. Increase of lattice strain with increasing doping concentrations at 2 h ball milled sample (inset).

field. Similar coexistence of ferromagnetism and paramagnetism has been observed in earlier cases of DMS samples [40,41–43]. As the particle size of DMS powders is in the nano scale regime, some of the particles could behave superparamagnetically. The origin of paramagnetism seems to develop from some isolated Mn^{2+} ions, which do not take part in ferromagnetism at room temperature. Spins of these isolated Mn^{2+} ions tend to align along the direction of the applied magnetic field giving rise to paramagnetic component. Small value of the coercive field and resulting small hysteresis area are quite similar to those of other ferromagnetic ZnO based DMS and nanocrystalline DMS-QD (quantum dot) aggregates [40,44–46]. Normally, for magnetic materials at relatively low temperatures a better signal is expected due to better magnetic ordering which is in accordance with our findings.

The origin of ferromagnetism in DMSs challenges our basic understanding of ferromagnetism. Most of the models assume a high density of charge carriers in the conduction, valence, or some impurity band within the band gap as a prerequisite to obtain room temperature ferromagnetism (RTF). The absence of any impurity phase, confirmed from the detailed XRD and HRTEM analysis, rules out the possibilities of ferromagnetism due to any extrinsic origin. If we exclude the possibility of an extrinsic origin, viz. ferromagnetic impurity segregation, then we can consider it as intrinsic in origin derived from the substitution of Mn^{2+} for Zn^{2+} ions retaining the wurtzite structure of ZnO. In the carrier mediated exchange mechanisms pertinent to magnetism, defects are important to the ferromagnetism of DMSs [46,47]. Many authors [19,48] including Sato and Katayama-Yoshida [49] proposed that uncontrolled formation of lattice defects can generate carriers that mediate ferromagnetic ordering. The idea of defect-mediated RTF has already been applied to Mn doped $CdGeP_2$ system [50,51]. As native point defects, oxygen vacancies are very common in ZnO and they contribute to the observed ferromagnetism in Mn doped ZnO [52–54]. However, oxygen vacancies in ZnO lattice have been critically examined through the structure and microstructure refinement of Mn-doped ZnO lattice by the Rietveld method. It is worthy noting that the oxygen vacancy in ZnO lattice is insignificant and may not play any role in defect-mediated RTF. The ferromagnetism in DMS materials has also been explained by the RKKY model [55] where the magnetism arises due to the exchange interaction between local spin-polarized electrons (in the present case, electrons of Mn^{2+} ions) and conduction electrons. It thus appears that population of free carriers plays an important role in manifestation of ferromagnetic property in these materials. The increasing

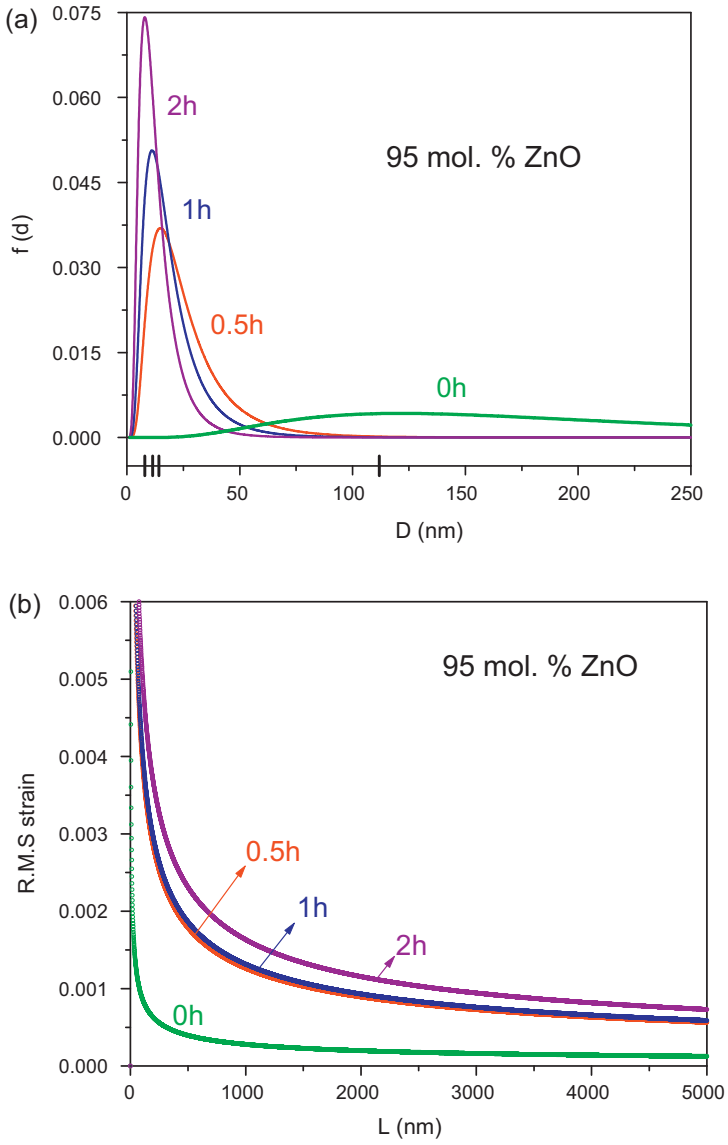

Fig. 10. (a) Distribution of particle sizes of ZnO with increasing milling time for one of the Mn concentrations ($x = 0.05$), (|) marks on the x-axis represents the most probable values of the particle sizes, (b) distribution of lattice strain of ZnO with increasing milling time for one of the Mn concentrations ($x = 0.05$).

value of the saturation magnetizations in the M-H curve is due to the orientation of the more number of polarized electrons in the direction of the applied magnetic field via conduction electrons by an indirect exchange interaction (RKKY) with increasing applied magnetic field.

The present investigation shows that the observed ferromagnetic interaction in the samples is primarily due to substitution of Mn^{2+} ions at regular Zn^{2+}sites in ZnO lattice. This result is in contrast to some earlier reports [56–60]. Kolesnik and Dabrowski [58] did not observe any ferromagnetic interaction in the bulk samples with composition $Zn_{1-x}Mn_xO$ ($x \leq 5\%$) synthesized by solid-state reaction method.

In the present study, DC magnetizations as a function of magnetic field show that the T_cs of RTF are well above the room temperature for all members of $Zn_{1-x}Mn_xO$ ($x \leq 10\%$) series. Our results clearly indicate that the observed ferromagnetism above RT for Mn doped ZnO samples is due to the incorporation of Mn^{2+} ions in ZnO lattice dominated by RKKY exchange interaction, rather than due to any impurity phase or oxygen vacancies in ZnO lattice.

4.4. Optical characterization

The optical absorption spectra of all these ball milled samples are obtained in the wavelength range (300–700) nm, depicted in Fig. 13(a). The coefficient of absorption of these samples is expected to depend on several factors, such as, surface roughness, dispersion effect, etc. The low value of absorption coefficients in case of $Zn_{1-x}Mn_xO$ may be due to light scattering at the rough surface of the particles. In the absorption spectra the maximum absorbed wavelength appears at ~377.5 nm for $x = 0.10$ and that for $x = 0.02$ appears at ~372 nm. It indicates that the absorption edges are in ultra-violet region and shift toward longer wavelength region with increasing values of x, i.e. a significant red-shift is clearly observed with increasing Mn content. The optical band gap energy of all these samples are calculated using Tauc [61] formula applicable for direct band gap semiconductors and plotted in Fig. 13(b).

The absorption edges of the samples are found to shift toward the longer wavelength side, which may be attributed to absorption of higher energy activation of sp-d exchange interaction. The values of the band gaps are found to decrease from ~3.336 eV to ~3.285 eV

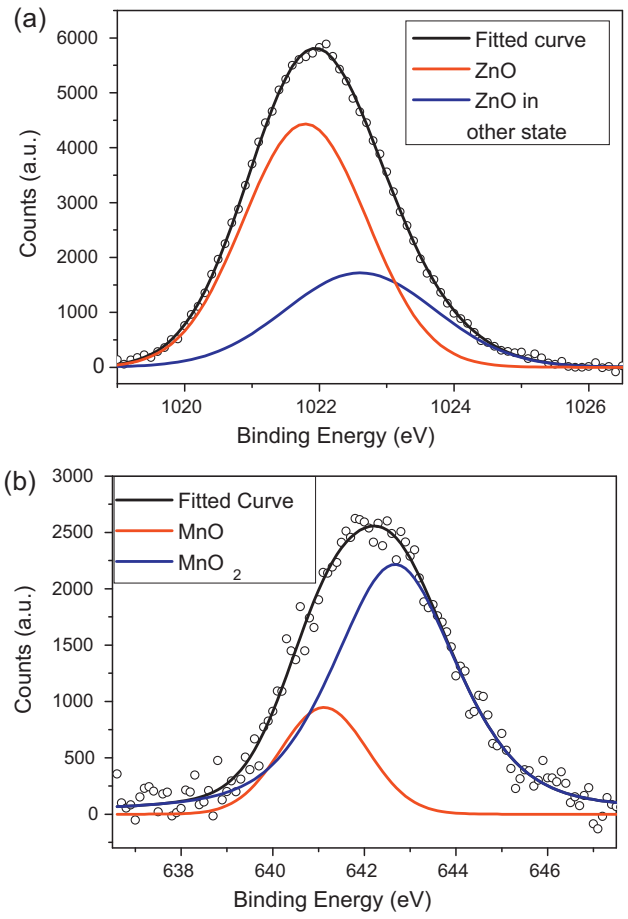

Fig. 11. (a) Typical Zn $2p_{3/2}$ and (b) Mn $2p_{3/2}$ XPS spectra of the 10 at.% Mn doped nano powders.

with corresponding increase in Mn concentration from $x = 0.02$ to 0.10, respectively, as shown Fig. 13(b). Similar phenomenon of decrease in band gap with increase in Mn content in ZnO is also observed in some previous reports also [62–65]. Similar type of behavior has been reported in case of Co doped ZnO films by Kim and Park [66], which is because of absorption of higher energy photons causes activation of 'spd' exchange interactions. This nature of

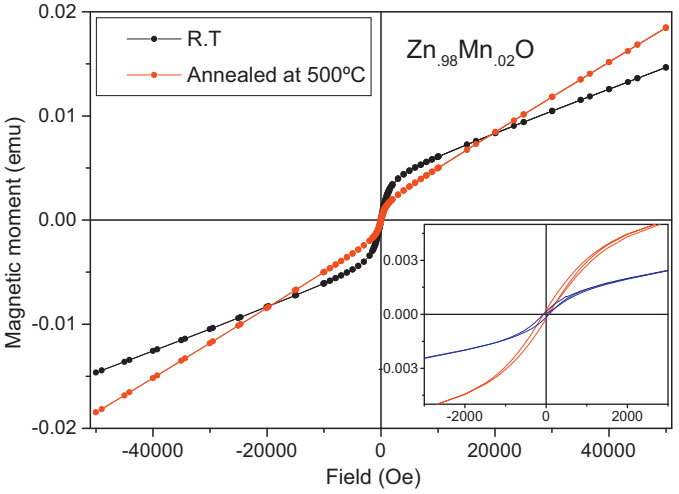

Fig. 12. Room-temperature magnetic hysteresis loop (M-H curve) of the Mn-doped ZnO nano powders.

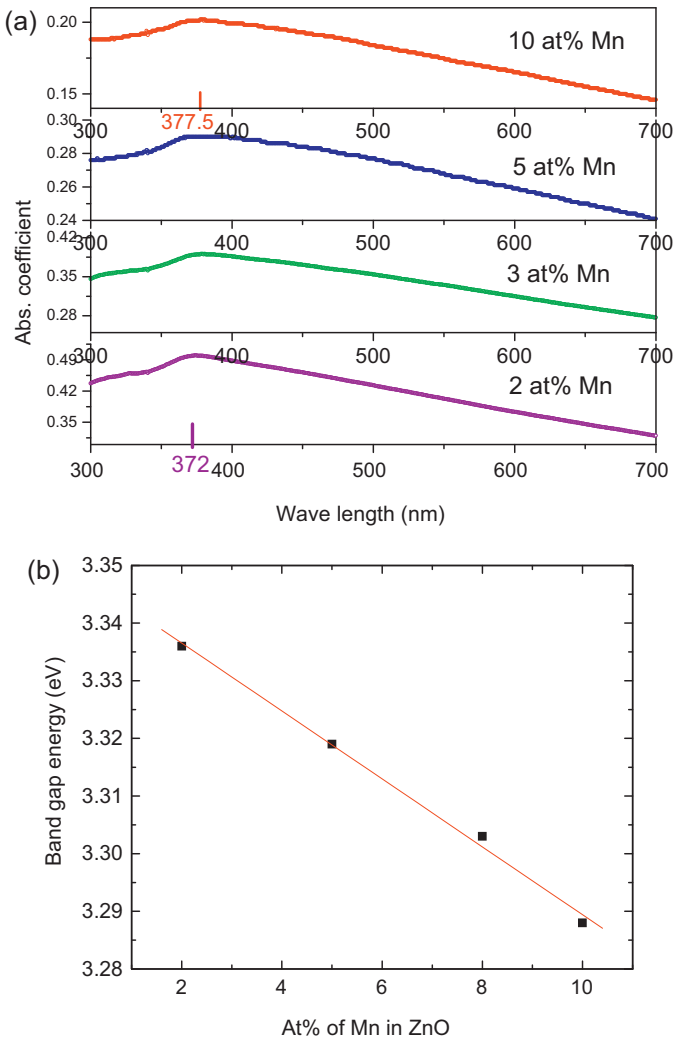

Fig. 13. (a) Variation of optical absorbance in different Mn doped ZnO DMSs. (b) Variation of optical band-gap with increasing Mn concentrations.

variation of band gap with Mn content may be attributed to the s–d and p–d interactions and it has been explained theoretically using the second order perturbation theory [63]. The observed decrease in the band gap can be explained with help of sp-d exchange interaction, which is a manifestation of strong exchange interaction present between d electron of Mn and the s and p electrons of host matrix. Although exchange interaction is more important in the presence of an external magnetic field H, in certain cases it can manifest at $H = 0$. However Fukumura et al. [67] has reported an overall blue shift in the band gap with increase in Mn concentration in thin epitaxial films on Mn doped ZnO and the reason for the blue shift was attributed to the higher band gap energy on MnO.

5. Conclusions

In conclusion, the above observations clearly reveal the following facts about the $Zn_{1-x}Mn_xO$ DMSs synthesized by mechanical alloying ZnO and MnO powder precursors:

(1) Nanocryatalline (~7 nm) $Zn_{1-x}Mn_xO$ with different doping concentration ($x = 0.02, 0.05, 0.07, 0.10$) are prepared successfully for the first time by mechanical alloying the stoichiometric mixture of ZnO and MnO powders at room temperature in a planetary ball within 2 h of milling.

(2) Detailed microstructure characterization of ball milled $Zn_{1-x}Mn_xO$ powders by Rietveld method of structure refinement reveals the incorporation of Mn into ZnO matrix, which means that the Mn^{2+} ions have substituted the Zn^{2+} ions without changing the wurtzite structure of ZnO. HRTEM images also corroborate the incorporation of Mn into ZnO matrix.
(3) Particle size of the prepared $Zn_{1-x}Mn_xO$ can be controlled with doping concentrations.
(4) Nanocrystalline DMS samples are free from any kind of contamination.
(5) XPS measurements indicate that the doped Mn ions possess both Mn^{2+} and Mn^{4+} valance states.
(6) SQUID measurements confirm the presence of RTF along with a paramagnetic component in both ball milled and annealed DMS samples.
(7) The observed decrease in the band gap of ZnO with increasing doping concentration is explained in terms of sp-d exchange interaction.

Acknowledgments

We wish to thank the University Grants Commission (UGC) India, for granting the "Centre of Advanced Study" programme under the thrust area "Condensed Matter Physics including Laser applications" to the Department of Physics, Burdwan University under the financial assistance of which the work has been carried out. One of the authors S. Sain also wishes to thank University Grants Commission (UGC) for providing research fellowship to carry out the research work.

References

[1] R. Kumar, F. Singh, B. Angadi, J.W. Choi, W.K. Choi, K. Jeong, J.H. Song, M.W. Khan, J.P. Srivastava, A. Kumar, R.P. Tandon, J. Appl. Phys. 100 (2006) 113708-1–113708-5.
[2] B.K. Meyer, H. Alves, D.M. Hofmann, W. Kriegseis, D. Forster, F. Bertram, J. Christen, A. Hoffmann, M. Straßburg, M. Dworzak, U. Haboeck, A.V. Rodina, Phys. Status Solidi B 241 (2004) 231–260.
[3] G. Lawes, A.S. Risbud, A.P. Ramirez, R. Seshadri, Phys. Rev. B 71 (2005) 045201–045205.
[4] A.M. Nazmul, S. Kobayashi, S. Sugahara, M. Tanaka, Physica E 21 (2004) 937–942.
[5] T. Jungwirth, K.Y. Wang, J. Mašek, K.W. Edmonds, J. König, J. Sinova, M. Polini, N.A. Goncharuk, A.H. MacDonald, M. Sawicki, A.W. Rushforth, R.P. Campion, L.X. Zhao, C.T. Foxon, B.L. Gallagher, Phys. Rev. B 72 (2005) 165204–165216.
[6] P. Sharma, A. Gupta, K.V. Rao, F.J. Owens, R. Sharma, R. Ahuja, J.M.O. Guillen, B. Johansson, G.A. Gehring, Nat. Mater. 2 (2003) 673–677.
[7] O.D. Jayakumar, I.K. Gopalakrishnan, S.K. Kulshrestha, Physica B 381 (2006) 194–198.
[8] K. Ueda, H. Tabata, T. Kawai, Appl. Phys. Lett. 79 (2001) 988–990.
[9] G.T. Thaler, M.E. Overberg, B. Gila, R. Frazier, C.R. Abernathy, S.J. Pearton, J.S. Lee, S.Y. Lee, Y.D. Park, Z.G. Khim, J. Kim, F. Ren, Appl. Phys. Lett. 80 (2002) 3964–3966.
[10] K. Sato, H.K. Yoshida, Physica B 308–310 (2006) 904–907.
[11] S.A. Chambers, T. Droubay, C.M. Wang, A.S. Lea, R.F.C. Farrow, L. Folks, V. Deline, S. Anders, Appl. Phys. Lett. 82 (2003) 1257–1259.
[12] J.H. Kim, H. Kim, D. Kim, Y. Eon, I. Woong, K. Choo, J. Appl. Phys. 92 (2002) 6066–6071.
[13] D. Milivojević, J. Blanuša, V. Spasojević, V. Kusigerski, B. Babić-Stoji, Solid State Commun. 141 (2007) 641–644.
[14] M. Ivill, S.J. Pearton, Y.W. Heo, J. Kelly, A.F. Hebard, D.P. Norton, J. Appl. Phys. 101 (2007) 123909-1–123909-5.
[15] J. Zhang, R. Skomski, D.J. Sellmyer, J. Appl. Phys. 97 (2005) 10D303-1–10D303-3.
[16] A. Chartier, P. D'Arco, R. Dovesi, V.R. Saunders, Phys. Rev. B 60 (1999) 14042–14048.
[17] S.A. Wolf, D.D. Awschalon, R.A. Buhrman, J.M. Daughton, S. von Molnar, M.L. Roukes, A.Y. Chtchelkanova, D.M. Treger, Science 294 (2001) 1488–1495.
[18] S. Chattopadhyay, S. Dutta, A. Banerjee, D. Jana, S. Bandyopadhyay, S. Chattopadhyay, A. Sarkar, Physica B 404 (2009) 1509–1514.
[19] T. Dietl, H. Ohno, F. Matsukura, J. Cibert, D. Ferrand, Science 287 (2000) 1019–1022.
[20] L. Lutterotti, P. Scardi, P. Maistrelli, J. Appl. Crystallogr. 25 (1992) 459–462.
[21] H.M. Rietveld, Acta Crystallogr. 22 (1967) 151–152.
[22] H.M. Rietveld, J. Appl. Crystallogr. 2 (1969) 65–71.
[23] R.A. Young, D.B. Willes, J. Appl. Crystallogr. 15 (1982) 430–438.
[24] L. Lutterotti, Maud Version 2.26. http://www.ing.unitn.it/~maud/ (accessed 28.02.11).
[25] E.J. Mittemeijer, P. Scardi, Diffraction Analysis of the Microstructure of Materials, Springer, Germany, 2004.
[26] S.K. Pradhan, M. Sinha, J. Appl. Crystallogr. 38 (2005) 951–957.
[27] S. Bid, P. Sahu, S.K. Pradhan, Physica E 39 (2007) 175–184.
[28] H. Dutta, M. Sinha, Y.C. Lee, S.K. Pradhan, Mater. Chem. Phys. 105 (2007) 31–37.
[29] M. Sinha, H. Dutta, S.K. Pradhan, Jpn. J Appl. Phys. 47 (2008) 8667–8672.
[30] B. Ghosh, S.K. Pradhan, J. Alloys Compd. 477 (2009) 127–132.
[31] S. Karamat, S. Mahmood, J.J. Lin, Z.Y. Pan, P. Lee, T.L. Tan, S.V. Springham, R.V. Ramanujan, Appl. Surf. Sci. 254 (2008) 7285–7289.
[32] M. Diaconu, H. Schmidt, H. Hochmuth, M. Lorenz, G. Benndorf, J. Lenzner, D. Spemann, A. Setzer, K.W. Nielsen, P. Esquinazi, M. Grundmann, Thin Solid Films 486 (2005) 117–121.
[33] J.F. Fernández, A.C. Caballero, M. Villegas, S.J. Khatib, M.A. Bañares, J.L.G. Fierro, J.L. Costa-Kramer, E. Lopez-Ponce, M.S. Martín-González, F. Briones, A. Quesada, M. García, A. Hernando, J. Eur. Ceram. Soc. 26 (2006) 3017–3025.
[34] V.K. Sharma, R. Xalxo, G.D. Varma, Cryst. Res. Technol. 42 (2007) 34–38.
[35] R.K. Singhal, M. Dhawan, S. Kumar, S.N. Dolia, Y.T. Xing, E. Saitovitch, Physica B 404 (2009) 3275–3280.
[36] J.H. Yang, L.Y. Zhao, Y.J. Zhang, Y.X. Wang, H.L. Liu, M.B. Wei, Solid State Commun. 143 (2007) 566–569.
[37] O.D. Jayakumar, I.K. Gopalakrishnan, C. Sudakar, R.M. Kadam, S.K. Kushreshtha, J. Alloys Compd. 438 (2007) 258–262.
[38] H. Zhou, D.M. Hofmann, A. Hofstaetter, B.K. Meyer, J. Appl. Phys. 94 (2003) 1965–1968.
[39] W. Xu, Y. Zhou, X. Zhang, D. Chen, Y. Xie, T. Liu, W. Yan, S. Wei, Solid State Commun. 141 (2007) 374–377.
[40] O.D. Jayakumar, I.K. Gopalakrishnan, R.M. kadam, A. Vinu, A. Asthana, A.K. Tyagi, J. Cryst. Growth 300 (2007) 358–363.
[41] H. Ohno, H. Munekata, T. Pandey, S.V. Molnar, L.L. Chang, Phys. Rev. Lett. 68 (1992) 2664–2667.
[42] G.Y. Ahn, S.I. Park, I.B. Shim, C.S. Kim, J. Magn. Magn. Mater. 282 (2004) 166–169.
[43] D.A. Schwartz, K.R. Kittilstved, D.R. Gamlein, Appl. Phys. Lett. 85 (2004) 1395–1397.
[44] N.S. Norberg, K.R. Kittilstved, J.E. Amonette, R.K. Kukkadapu, D.A. Schwartz, D.R. Gamelin, J. Am. Chem. Soc. 126 (2004) 9387–9398.
[45] P.V. Radovanovic, D.R. Gamelin, Phys. Rev. Lett. 91 (2003) 157202.
[46] J.M.D. Coley, M. Venkatesan, C.B. Fitzgerld, Nat. Mater. 4 (2005) 173–179.
[47] T. Meron, G. Markovic, J. Phys. Chem. B 109 (2005) 20232–20236.
[48] T. Dietl, Semicond. Sci. Technol. 17 (2002) 377–392.
[49] K. Sato, H. Katayama-Yoshida, Semicond. Sci. Technol. 17 (2002) 367–376.
[50] P. Madhavan, A. Zunger, Condens. Matter (2001), 0111570.
[51] G.A. Medvedkin, T. Ishibashi, T. Nishi, K. Hayata, Y. Hasegawa, K. Sato, Jpn. J. Phys. 39 (part 2) (2000) L949–L951.
[52] P. Long, Z.H. Wu, W.Q. Ye, S.Y. Qiang, S. Hua, J.Q. Xiao, Chin. Phys. Lett. 25 (2008) 1438–1441.
[53] N.H. Hong, J. Sakai, N.T. Huong, N. Poirot, A. Ruyter, Phys. Rev. B 72 (2005) 045336-1–045336-5.
[54] A. Sundaresan, R. Bhargavi, N. Rangarajan, U. Siddesh, C.N.R. Rao, Phys. Rev. B 74 (2006) 161306-1–161306-4.
[55] D.J. Priour Jr., E.H. Hwang, S.D. Sharma, Phys. Rev. Lett. 92 (2004) 117201-1–117201-4.
[56] S.J. Han, T.H. Jang, Y.B. Kim, B.G. Park, J.H. Park, Y.H. Jeong, Appl. Phys. Lett. 83 (2003) 920–922.
[57] W. Chen, L.f. Zhao, Y.Q. Wang, J.H. Miao, S. Liu, Z.C. Xia, S.L. Yuan, Appl. Phys. Lett. 87 (2005) 042507-1–042507-3.
[58] S. Kolesnik, B. Dabrowski, J. Appl. Phys. 96 (2004) 5379–5381.
[59] D.P. Joseph, G.S. Kumar, C. Venkateswaran, Mater. Lett. 59 (2005) 2720–2724.
[60] C.N.R. Rao, F.L. Deepak, J. Mater. Chem. 15 (2005) 573–578.
[61] J. Tauc, Amorphous and Liquid Semiconductor, Plenum Press, New York, 1974, p.159.
[62] Y. Guo, X.B. Cao, X.M. Lan, C. Zhao, X.D. Xue, Y.Y. Song, J. Phys. Chem. C 112 (2008) 8832–8838.
[63] R.B. Bylsma, W.M. Becker, J. Kossut, U. Debska, Phys. Rev. B 33 (1986) 8207–8215.
[64] H.W. Zhang, E.W. Shi, Z.Z. Chen, X.C. Liu, B. Xiao, L.X. Song, J. Magn. Magn. Mater. 305 (2006) 377–380.
[65] P. Singh, A. Kaushal, D. Kaur, J. Alloys Compd. 471 (2009) 11–15.
[66] K.J. Kim, Y.R. Park, Appl. Phys. Lett. 81 (2002) 1420–1422.
[67] T. Fukumura, Z. Jin, A. Ohtomo, H. Koinuma, M. Kawasaki, Appl. Phys. Lett. 75 (1999) 3366–3368.